High-speed stereo DPIV measurement of wakes of two bat species flying freely in a wind tunnel

Anders Hedenström · F. T. Muijres · R. von Busse · L. C. Johansson · Y. Winter · G. R. Spedding

Abstract Previous studies on wake flow visualization of live animals using DPIV have typically used low repetition rate lasers and 2D imaging. Repetition rates of around 10 Hz allow ~ 1 image per wingbeat in small birds and bats, and even fewer in insects. To accumulate data representing an entire wingbeat therefore requires the stitching-together of images captured from different wingbeats, and at different locations along the wing span for 3D-construction of wake topologies. A 200 Hz stereo DPIV system has recently been installed in the Lund University wind tunnel facility and the high-frame rate can be used to calculate all three velocity components in a cube, whose third dimension is constructed using the Taylor hypothesis. We studied two bat species differing in body size, *Glossophaga soricina* and *Leptonycteris curasoa.* Both species shed a tip vortex during the downstroke that was present well into the upstroke, and a vortex of opposite sign to the tip vortex was shed from the wing root. At the transition between upstroke/downstroke, a vortex loop was shed from each wing, inducing an upwash. Vorticity iso-surfaces confirmed the overall wake topology derived in a previous study. The measured dimensionless circulation, Γ/Uc, which is proportional to a wing section lift coefficient, suggests that unsteady phenomena play a role in the aerodynamics of both species.

A. Hedenström (✉) · F. T. Muijres · L. C. Johansson
Department of Theoretical Ecology, Lund University,
Ecology Building, 223 62 Lund, Sweden
e-mail: Anders.Hedenstrom@teorekol.lu.se

R. von Busse · Y. Winter
Department of Biology, Bielefeld University,
33501 Bielefeld, Germany

G. R. Spedding
Department of Aerospace and Mechanical Engineering,
University of Southern California, Los Angeles,
CA 90089-1191, USA

Present Address:
G. R. Spedding
Department of Mechanical and Aeronautical Engineering,
University of Pretoria, Pretoria 0002, South Africa

1 Introduction

Flapping flight in vertebrates has resisted simple analysis, because of the time-varying shape of elastic actuators and their complex interaction with the surrounding fluid. Early models therefore discarded these facts altogether by representing the animal, bird or bat, by mass and wing span alone (Pennycuick 1968, 1975; Norberg 1990). Even though this approach allows predictions for cruising flight performance (Pennycuick 1989; Hedenström 2002), it does not capture any details of the kinematics and associated time-varying force production and cannot be used to predict performance during maneuvering or hovering flight. On the other hand, the early vortex wake theory of bird flight was based upon a minimum of kinematic details, even if the assumptions about the wake geometry itself were more realistic than the actuator disk and momentum jet models (Rayner 1979a, b). Experiments originally focused upon kinematic analyses of wing motions (Brown 1948; Norberg 1976; Aldridge 1986). Eventually, with improved experimental techniques for quantitative wake flow visualization (Spedding et al. 1984; Spedding 1987a, b), the conceptual image of the wake structure began to improve (if not always simplify), now that it was based on actual evidence. Digital particle image velocimetry (DPIV) techniques have been applied to freely flying birds in wind

G.K. Taylor, M.S. Triantafyllou, and C. Tropea (Eds.): Animal Locomotion, pp. 361–370.
springerlink.com

tunnels (Spedding et al. 2003a, b; Warrick et al. 2005; Hedenström and Spedding 2008) to yield more refined models of the wake geometry and its variation with forward flight speed, wing geometry and kinematics. The same techniques have also been applied to the small Glossophagine bats, and reveal some notable differences in wake geometry compared with birds (Hedenström et al. 2007).

To date, quantitative wake data of flying vertebrates have come from rather low repetition rates lasers (5–10 Hz), and the three-dimensional wake structure over one wingbeat cycle is assembled from large numbers of separate images, obtained from large numbers of separate wingbeats. Previous studies have also derived primarily from stacks (in space or time) of 2D data, with two out of three velocity components available in any one plane. Nevertheless, the use of DPIV methods has considerably strengthened our understanding of wake topology and aerodynamics of vertebrate flapping flight in recent years (e.g. Hedenström and Spedding 2008), and continued rapid technological advances are likely to propel the scientific progress further still (see Spedding and Hedenström 2009, this issue). Here we report on the first high-speed stereo-3D DPIV measurements, and thus 3D velocity profiles, of bat flight in the Lund University wind tunnel using two species of Glossophagine bats. The main objective was to investigate whether the wake topology derived from high-speed wake sampling conforms to previous conclusions derived from low-speed sampling (Hedenström et al. 2007). A second objective was to compare the scaling of wake properties from two species of bats with different body weight, aspect ratio and wing loading.

2 Materials and methods

2.1 Experimental animals

Two species of nectarivorous bats, *Glossophaga soricina* and *Leptonycteris curasoae*, were trained to fly in front of a thin metal tube (feeder) providing honey water in the test section of a low-turbulence wind tunnel. For these experiments, two individuals each of *G. soricina* and *L. curasoae* were used. The morphology of the four bats is summarised in Table 1. Wing span and wing area were measured from top-view images obtained at flight speeds 5–6 m/s captured, when the wings are positioned horizontally during the downstroke. At this flight speed, the body angle is near horizontal. Wing span and wing area were measured using ImageJ (http://rsb.info.nih.gov/ij/) with the length of the radius as reference length (Table 1). Body mass was measured with an electronic balance before and after each experimental session, and the mean values are shown in Table 1.

Since bats are nocturnal and mainly active in the dark, they were clock-shifted by 12 h, so their active feeding period coincided with researchers' working schedule. Before experiments, the bats were released into the wind tunnel, where they roosted on a net inside the settling chamber 6 m upstream from the test section. When a bat decided to feed, it would fly with the wind towards the test section, increasing the speed between the settling chamber and the test section through the contraction, and would then make a U-turn inside the test section to approach the feeder from the downstream direction. The requirement of making this U-turn inside the test section area (1.22×1.08 m) limits the maximum flight speed range that can be studied to approximately 7–8 m/s.

2.2 Wind tunnel

The Lund University wind tunnel is a closed-loop, low-speed, low-turbulence wind tunnel crafted for studies of animal flight. The overall design and baseline characteristics are described in Pennycuick et al. (1997). The background turbulence is about 0.03% (Spedding et al. 2009), which makes this tunnel suitable for repeatable quantitative measurements at the moderate values of wing chord-based Reynolds number that are characteristic of small birds and bats (see below). All airspeeds (U) refer to the equivalent airspeed defined as

$$U_{\mathrm{eq}} = \sqrt{2q/\rho_0},$$

Table 1 Morphological properties of the four bats used in this study, body mass (m), wing span (b), wing area (S), mean wing chord (c), aspect ratio (AR $= b^2/S$), wing loading ($Q = mg/S$), and f is wing beat frequency

Bat	m (kg)	Femur length (mm)[a]	Wing length (m)	b (m)	S (m^2)	c (m)	AR	Q (N)	f (Hz)
Glossophaga soricina, male (#1)	0.0101	34.6	0.101	0.233	0.00879	0.038	6.2	11.3	14.9
Glossophaga soricina, female (#5)	0.0095	34.9	0.097	0.230	0.00860	0.037	6.2	10.9	14.9
Leptonycteris curasoae, male (#97)	0.0216	50.3	0.149	0.335	0.01576	0.047	7.1	13.4	10.4
Leptonycteris curasoae, female (#18)	0.0236	51.0	0.144	0.323	0.01529	0.047	6.8	15.1	9.9

[a] Used as reference length on images for estimating wing length, wing span and wing area

where ρ_0 is the assumed air density at sea level in the International Standard Atmosphere (1.225 kg/m^3) and q ($=\rho U^2/2$) is the dynamic pressure at the measured air density during an experiment. During this study, ρ varied between 1.16 and 1.20 kg/m^3, and the temperature was 19–24°C. The bats were studied at forward flight speeds 1–7 m/s, but the main results in this paper are based on observations at 4 m/s. The Reynolds number based on airspeed ($Re = Uc/v$, where c is the mean chord length of the wing and v is the kinematic viscosity) ranged from $Re = 0.26–1.81 \times 10^4$ in *G. soricina* to $Re = 0.32–2.27 \times 10^4$ in *L. curasoae*. At $U = 4$ m/s, the speed for which we present most of the data in this paper, $Re = 1.03 \times 10^4$ and 1.30×10^4, respectively. This difference in Re is aerodynamically not significant. The bats are small in comparison with the test section [wing span (b)/tunnel diameter (B): $b/B < 0.28$) and so interactions with the side walls are ignored.

2.3 Stereo DPIV

The flow field was measured over an approximately 20×20 cm^2 area using two CMOS-cameras (HiSpeedStar3; 1,024 × 1,024 pixels) and frame grabber PCI boards in the host computer. The cameras were equipped with 60 mm lenses (Micro Nikkor, f2.8) on Scheimpflug mounts. Two alignments of the light sheet were used: (1) the vertical [xz] plane is aligned with the free-stream, with the cameras mounted on opposite sides outside the test section (Fig. 1a), and (2) the [yz] plane is normal to U, and the cameras are mounted in the open part of the test section (Fig. 1b), viewing obliquely from above and behind onto

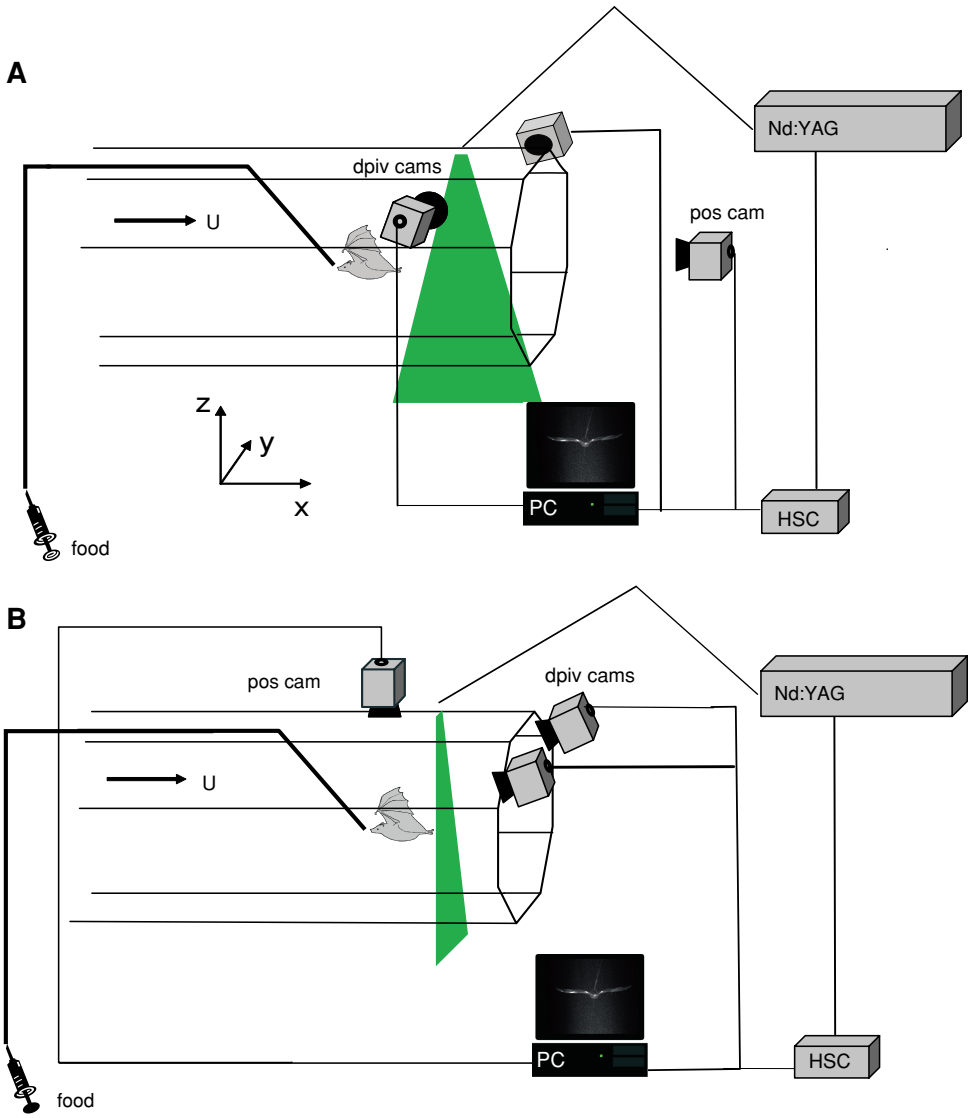

Fig. 1 Experimental set-up for visualizing wakes of bats flying in the Lund University wind tunnel. The pulsed laser (Nd:YAG) generates a light sheet in the wind tunnel test section. Image pairs of densely-distributed fog particles, illuminated by the light sheet, are captured by the two CMOS cameras (DPIV cam) and stored on the host PC. The light sheet is positioned by the use of an optical arm and either aligned parallel to U (**a**) or perpendicular to U (**b**). The position camera monitors the flight behaviour and position of the bat with respect to the light sheet. The triggering of image acquisition and laser pulses is synchronized by a high speed controller box (HSC). Honey water is provided through a syringe and thin plastic tubing to a metal tube of 3 mm diameter

the light sheet. The feeder was about 20 cm upstream of the center of the light sheet, and the distance from the wing tip to the imaging plane varied between 16 and 18 cm, which is 3.4–4.7c, or 0.5–0.8b. At $U = 4$ m/s, the vortex travel time from the wing tip to the imaging plane was about 0.04 s, which is 0.4–0.6T_w, where T_w is the time for one wingbeat cycle. The whole tunnel was filled with a thin fog (particle size 1 μm), which was illuminated in slices by a pulsed 50 mJ Laser (Litron LPY732 series, Nd:YAG, 532 nm) at 200 Hz repetition rate. The PIV cameras have band pass filters (530 ± 5 nm) to minimize stray light from other sources. An independent camera monitored the position and flight behaviour of the bat in relation to the light sheet. This position-monitor camera was positioned on the top of the test section in the transverse light sheet configuration (Fig. 1b), and in the first diffuser downstream from the test section in the streamwise light sheet configuration (Fig. 1a). For both transverse [yz] and streamwise [xz] data, the left wing and body were imaged.

2.4 DPIV analysis

2.4.1 The DPIV system and calibration

The DPIV data are captured and analyzed using the DaVis software package from LaVision (Davis 7.2.2.110). It is calibrated using a calibration plate (20 × 20 cm^2, type 22), in combination with the DaVis Stereo PIV self-calibration algorithms to compensate for misalignments between the laser sheet and the calibration plate. Background flow DPIV measurements were performed for monitoring the pixel displacement magnitudes and possible peak-locking errors, and the time difference between the laser pulses was adjusted to optimise the available velocity bandwidth. The background flow was also used to determine the flight speed at low wind tunnel speed settings ($U \leq 2$ m/s), since at these low speeds, the conventional wind tunnel monitor system (using the static pressure difference before and after the contraction immediately upstream from the test section) is inaccurate. At low speeds, the spatial variation (RMS within the 20 × 20 cm^2 measurement area) was less than 2.5% of the mean velocity ($n = 6$). The temporal velocity variations are on average of 2.25% of the mean velocity ($n = 3$), with a maximum time difference between the measurements of 1 h.

2.4.2 Data acquisition

The bat flight data were captured by manual triggering. When a bat was flying steadily in front of the feeder, the laser shutter was opened and a sequence of 50 frames was captured by the DPIV cameras. Simultaneously (using a synchronization signal), a 1 s video sequence of the flying bat and laser pulses was recorded using a 250 Hz frame-rate digital video camera (Fig. 1). If the bat continues to fly behind the feeder, the triggering routine can be repeated. This procedure typically generates DPIV data for up to two (*L. curasoae*) and three (*G. soricina*) consecutive wingbeats per trigger event.

2.4.3 Analysis

The DPIV data were analyzed using the DaVis software. The images were pre-processed to reduce systematic errors due to background noise, for example, when a bat is visible in the background. A multi-pass stereo cross-correlation was used (64 × 64 and 32 × 32, 50% overlap), and the results were post processed using a correlation peak ratio deletion scheme (peak ratio < 1.01), a median vector field filter, and a false vector rejection criterion of vector magnitudes, $|v| > 1.5$ times the neighbourhood RMS, and recalculation for $|v| > 2$ times the local RMS, and a single 3 × 3 smoothing average.

The computed $\{u, v, w\}$ velocity components in x- (streamwise), y- (spanwise) and z- (vertical) directions were used to calculate the vorticity components, $\{\omega_x, \omega_y, \omega_z\}$ normal to the planes [yz, zx, xy], respectively. For example, the streamwise vorticity, $\omega_x = \partial w/\partial y - \partial v/\partial z$, is determined by the $\{v, w\}$ velocity gradients in the [yz] plane. The circulation of identified vortex structures was also measured in selected planes using procedures described in Spedding et al. (2003b).

The DPIV data were compiled into a 3D spatial matrix (x, y, z), by concatenating the results from consecutive DPIV frames, and converting the time difference between the frame pairs into a streamwise displacement ($\Delta x = U\Delta t$). When doing this, one assumes that wake displacements are dominated by mean flow convection, and that no strong vortex wake evolution/kinematics occurs at and after the measurement point.

Although the data are assembled into a single 3D cube, the original data acquisition planes (where the in-plane velocity estimation errors are smaller than the out-of-plane components) have some particular interest in the analysis. The streamwise [xz] planes are parallel to U, and to g. The drag is defined as the aerodynamic force component parallel to U, and the lift is defined as normal to U, which is parallel to g here. The u and w disturbance velocities are therefore the leading contributors to estimates of D and L. Invoking quite reasonable assumptions for far-field flows shows that they are the only components of significance (see Spedding and Hedenström 2009, this volume). These points were noted in the original bird flight DPIV studies (Spedding et al. 2003b) and the [xz] plane data can be compared directly with them.

The [yz] plane, normal to U, is where the v and w components of velocity can be most accurately estimated

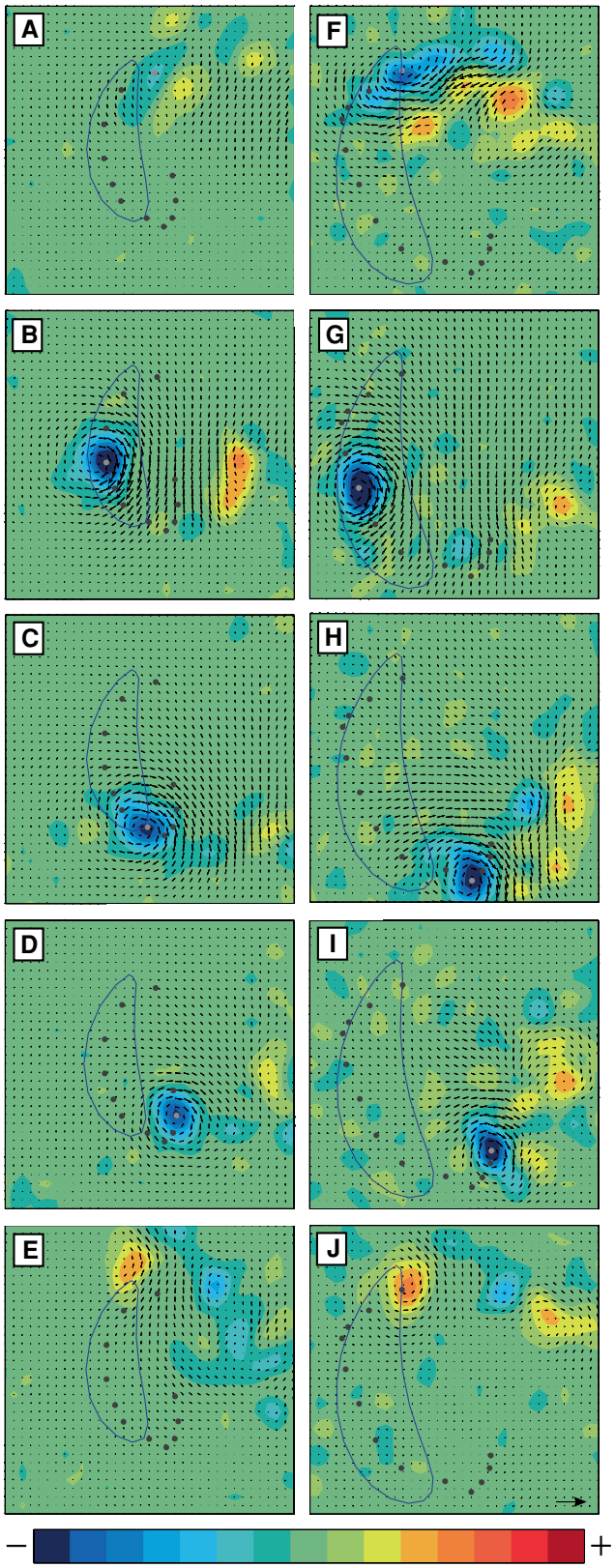

Fig. 2 Colour-coded vorticity fields and velocity vector fields from two bats flying in a wind tunnel. The images show the [*yz*] plane of the left wing and body for one *Glossophaga soricina* (**a**–**e**) and one *Leptonycteris curasoae* (**f**–**j**), both flying at $U = 4$ m/s. The individual bats are the males (#1 and #97) of Table 1. The distance from the bat to the [yz] imaging plane varied between 3.4 and 4.7 chord lengths. The *panels* represent sub-periods of a wing stroke as follows (*top–bottom*): beginning of downstroke, mid downstroke, end of downstroke, mid upstroke and end of upstroke. The colour scale symmetrically maps the streamwise vorticity, ω_x, (s^{-1}) from −280 (*blue*) to +280 (*red*) in steps of 40 s^{-1}. The {*v*,*w*}-component velocity vectors are scaled to the reference at 5 m/s at *bottom right*. The *closed curves* show the path of the wing tip for an average wingbeat and the *dots* show the centers of the wing tip vortices with the *grey dot* showing the current frame. The *panels* represent a real area of 17.5 × 17.5 cm

together. When this plane is far from the disturbance source, then the only significant disturbance velocities will be the *v* and *w* components in the wake itself (*u* will be much smaller), and inviscid theory can be used to estimate the induced drag of a wake oriented parallel to *U* and passing through this plane. This plane is called the Trefftz plane in aeronautics. If all the three components of velocity are available in this plane, then both the lift and drag can be computed, using only this information. It is tempting to invoke all [*yz*] planes as Trefftz planes, but they must be large, far from the body and the wake must be normal to them for the original analysis to hold.

3 Results

3.1 Wake structure and implications for aerodynamic force generation on the wing

Figure 2 shows a time sequence of [*yz*] planes at $x/c \approx 5$ (from set-up in Fig. 1b), behind the body and left wing through one complete wing stroke at $U = 4$ m/s, for one individual each of *G. soricina* and *L. curasoae* (hereafter *G. s.* and *L. c.*). The path of the wingtip is shown by a continuous line and the centers of the tip vortices are shown as black dots with the current centre of the wing tip vortex shown in grey. At the beginning of the downstroke, some weak streamwise vorticity is seen in *G. s.* (Fig. 2a), while in *L. c.*, the tip vortex is already visible (blue patch, Fig. 2f), together with a counter-rotating vortex shed from the wing root (yellow patch, Fig. 2f). By mid downstroke, there are prominent wing tip vortices as well as wing root vortices in both species (Fig. 2b, g). At this stage, there is a clear downwash between the opposite-signed shed vortices, with magnitude (mean ± SD) 1.47 ± 0.63 m/s ($n = 18$) and 1.27 ± 0.47 m/s ($n = 25$) in *G. s.* and *L. c.*, respectively (*n* is the number of vectors between tip- and toot-vortices). The larger sample size in *L. c.* is due to the longer wingspan compared with *G. c.* At mid downstroke, the wing span has its maximum horizontal extent, and the horizontal distance, l_y, between tip and root vortices for

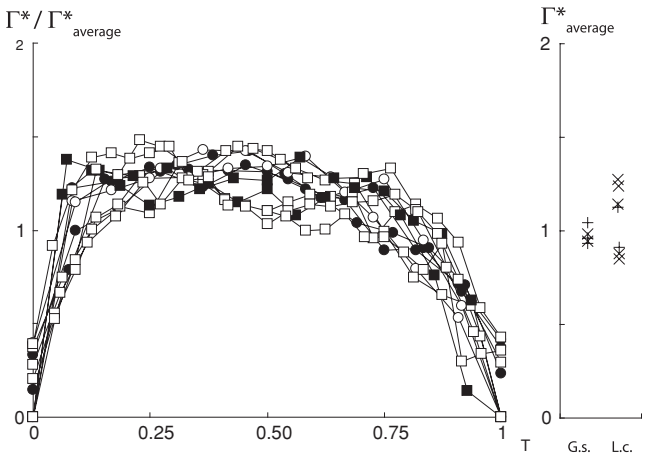

Fig. 3 Normalised circulation, $\Gamma^*_{\text{average}} = \Gamma/Uc$, of the wingtip trailing vortex, realtive to the mean value of the sequence. Mean values for individual wingbeats are given in the *panel* to the *right*. The *symbols* represent *Glossophaga soricina* (*circles*; *open* and *filled symbols* denote different individuals) and *Leptonycteris curasoae* (*squares*) followed over a number of wing strokes. The wingbeat period was 0.067 and 0.099 s for *Glossophaga soricina* and *Leptonycteris curasoae*, respectively

G. s. and *L. c*. is 7.9 and 12.2 cm, respectively. Normalised by the wing semispan, $2l_y/b = 0.69$ and 0.74, respectively.

At the end of the downstroke, the tip vortex has the same circulation magnitude as at mid downstroke, but it is now shed from a position closer to the body midline as the wing tips are moved towards each other below the body (Fig. 2c, h). At the beginning of the upstroke, the wing is being flexed and at mid upstroke, the tip vortex is still present, although it is closer to the body midline than it was at mid downstroke. Notice that there is still an induced downwash about halfway into the upstroke (Fig. 2d, i), indicating that the wing is generating lift also during the upstroke up to this point. Towards the end of the upstroke, the tip vortex vanishes, but instead, there is shedding of a vortex dipole inducing an upwash and hence an associated negative lift (Fig. 2e, j). The root vortex appears weaker during the upstroke in *G. s*. than in *L. c*. (Fig. 2c, d vs. h, i). In most cases, the centre of the tip vortex is inboard of the wing-tip trace, except for about one quarter into the downstroke in *L. c.* (Fig. 2).

The circulation, Γ is a measure of the integrated vorticity magnitude in a region. The normalised circulation of the tip vortices, $\Gamma^* = \Gamma/Uc$, is plotted as a function of T ($T = t/T_{\text{w}}$, where T_{w} is the wing beat period, and t is counted from the beginning of each downstroke) stroke at $U = 4$ m/s in Fig. 3. Γ^* increases rapidly after the beginning of the downstroke ($T < 0.1$), and then varies only little between 1.2–1.8 well into the upstroke ($T \approx 0.75$), after which it drops to almost zero at the end ($T = 1$) of the upstroke. The pattern and magnitude of the circulation variation throughout a wing stroke are very similar between the two species, although one individual *L. c.* (the female) appears to show somewhat larger variation.

3.2 Three-dimensional wake topology

As the wake is sampled at 200 Hz, the $[yz](t)$ image sequence can be used to generate iso-surfaces of constant streamwise vorticity (ω_x) over one wing stroke. $\omega_x(x, y, z)$ was assembled from time sequences of data, such as Fig. 2, using the previously-noted transform rule $\Delta x = U\Delta t$, and ω_x iso-surfaces are shown in Fig 4. The iso-values of ω_x are $\pm$mean $|\omega_x|$ (red positive, blue negative). The bat is flying from left to right and obliquely towards the observer, and the iso-surfaces show the streamwise vorticity that trails the bat wing and body during the course of a little over one wingbeat. The tip vortex shed by the right wing is blue, circulating clockwise when viewed downstream from the bat, and the root vortex is red, rotating in the opposite, anti-clockwise direction. Their counterparts in mirror image behind the left wing are opposite in direction of rotation and colour. The downstroke generates a prominent tip vortex in both *G. s.* and *L. c.* A wing root vortex of opposite sign is also present during the downstroke in both species. At the end of the upstroke, an inverted vortex dipole, whose cross-section was shown in Fig. 2e and j, can be seen in the top right of both Fig. 4a and b. The wingtip trailing vortex gradually loses strength and falls below the visualization threshold towards the end of the upstroke, but we should remember that the visualized component is ω_x (and not $|\omega|$), so although the connecting start and stop vortices, which are primarily ω_y, are not visible, their presence (as required by Helmholtz's conservation laws) is known from the full vorticity vector data, and from plots of ω_y (x, z). Here, however, the vortex loops appear as disconnected vortex strands of ω_x.

3.3 Wake defect maps

Figure 5 shows the normalized streamwise velocity, $(u - U)/U$. Since drag and thrust are associated with deceleration and acceleration of the mean streamwise velocity, U, then a region of $(u - U)/U < 0$ might be interpreted to contribute a net drag and $(u - U)/U > 0$, a net thrust. Then the integrated sum of these regions, taken over a suitable control volume, will be zero for any self-propelled body in steady motion. This is a rather over-simplified picture, especially for such a complex flow, and so close to the wings and body (see Spedding and Hedenström 2009, this volume, for conditions for estimating mean forces from wake velocity distributions), but as a first order approximation, we may assert that maps of $(u - U)/U$ show where the major contributors to thrust and drag are located on the bat, through their imprint in the cross-plane wake. The trailing tip vortex has a velocity defect towards its centre in both species. This

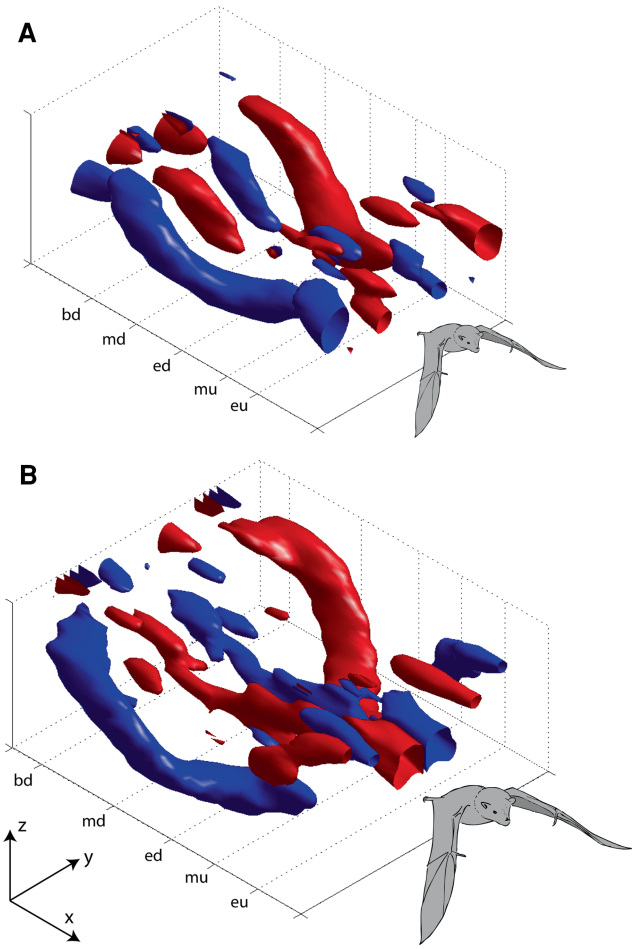

Fig. 4 Iso-surfaces of normalized constant streamwise vorticity ($\omega_x^* = \omega_x/|\varpi_x|$) during just over one wing stroke of (**a**) *Glossophaga soricina* (#1) and (**b**) *Leptonycteris curasoae* (#97). The iso-values are normalized of $\omega_x^* = \pm 1.0$ (*red* is positive; *blue* is negative). The data cubes are oriented, so the bat is flying obliquely to the right and towards the viewer. The larger centrally trailing tubes therefore mark the streamwise vorticity shed at the wing root. Approximate time-marks are: *bd* (beginning of downstroke), *md* (mid downstroke), *ed* (end of downstroke), *mu* (mid upstroke), *eu* (end of upstroke). The *data boxes* are scaled as (x, y, z) = (400, 260, 180) mm in (**a**) and (x, y, z) = (400, 345, 180) mm in (**b**)

is consistent with an axial flow along the vortex core towards the wing, as also noted in the kestrel wake by Spedding (1987b), and based also on 3D velocity fields. The strongest accelerated wake flow appears inboard of the tip vortex, between it and the wing root. At the body, the flow is again decelerated in this cut, at this stage of the wingbeat. Figure 6 shows that this is true for most of the wingbeat, for both bats.

4 Discussion

4.1 Aerodynamically-equivalent flight speeds

This paper describes the wakes of two species of bats flying at the same speed, $U = 4$ m/s, which is in the middle of the

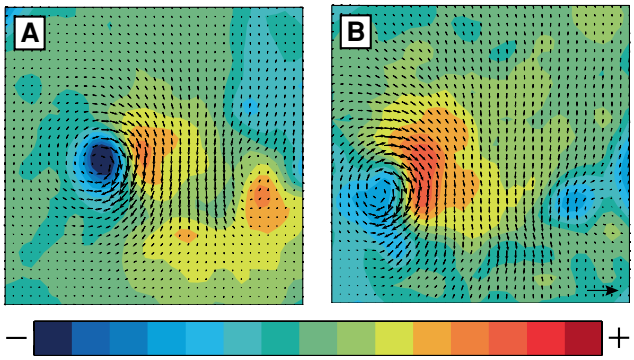

Fig. 5 $(u - U)/U$ at mid downstroke of (**a**) *Glossophaga soricina* (#1)and (**b**) *Leptonycteris curasoae* (#97). The *colour bar* runs from $(u - U)/U = -0.35$ to 0.35 in steps of 0.05 m/s. The $\{v,w\}$-component velocity vectors are scaled to the reference at 5 m/s at *bottom right*. The *panels* represent a real area of 17.5 × 17.5 cm

speed range of small bats (Lindhe Norberg and Winter 2006). In a comprehensive study of insect flight, Ellington (1984) used the advance ratio $J = U/2\Phi fR$, where Φ is stroke angle (in radians), f is wingbeat frequency and R is wing length, to describe the force asymmetry between downstroke and upstroke and defined hovering as including slow forward speed with $J < 0.1$. Here $J = 1.08$ for both for *G. s.* and *L. c.* The related Strouhal number, $St = fA/U$, where A is the vertical peak-to-peak amplitude of the wingtip, evaluates to 0.47 and 0.43 for *G. s.* and *L. c.*, respectively. The similar values of both J and St show that the flight speeds are aerodynamically-equivalent for the two bat species, even though they are of different size.

St measures the mean wingtip speed relative to the forward speed (it is one half of this ratio; Spedding et al. 2008) and so at $U = 4$ m/s, the tip and forward speeds have a similar magnitude. Since the wingtip speed fluctuates considerably during each wingbeat cycle, then we may expect time-varying aerodynamic force components to be non-negligible, simply based on such values of St.

4.2 The loading and unloading wing cycle

The circulation of the wingtip trailing vortex varies smoothly through the downstroke/upstroke transition and continues to be measurable, with the same sign, until close to the end of the upstroke. At the same time, a downwash induced between the wingtip and wing root sections supports the notion that the upstroke is aerodynamically active for about half its duration, at which point, the circulation falls to zero and the wing is aerodynamically unloaded. This cycle of wing loading and unloading through the wingbeat is quite consistent with previous interpretations (Hedenström et al. 2007) based on multiple 2D DPIV planes. The agreement of the 3D data with multiple 2D slices from hundreds of different wingbeats is gratifying.

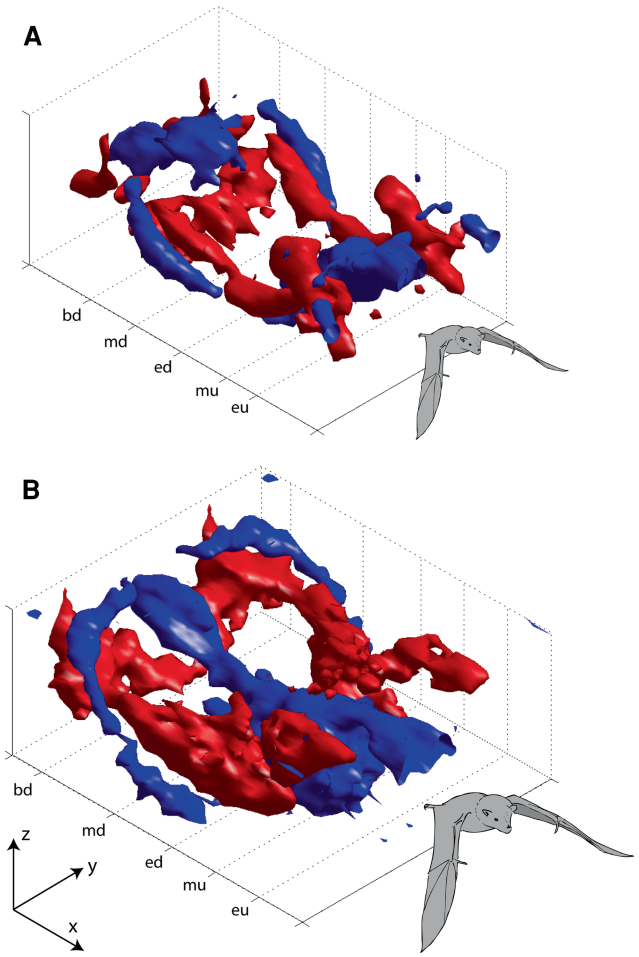

Fig. 6 $(u - U)/U$ (x, y, z) for one wing beat of (**a**) *Glossophaga soricina* (#1) and (**b**) *Leptonycteris curasoae* (#97). Orientation and time-marks as in Fig. 4.The threshold values used were $(u - U)/U = \pm 0.25$ in (**a**) and ± 0.3 in (**b**). The *data boxes* are scaled as $(x, y, z) = (400, 260, 180)$ mm in (**a**) and $(x, y, z) = (400, 345, 180)$ in (**b**)

4.3 Pseudo-3D data

It is not only the wing loading/unloading cycle that can be confirmed in the 3D data, but also the observations of wing root vortices and of the shedding of inverted vortex loops at the end of the upstroke. These phenomena were newly observed in bats and make their wake signatures qualitatively different from those of birds (Hedenström et al. 2007). The 3D reconstructions in Figs. 4 and 6 are reasonable if the transformation $\Delta x = U\Delta t$ is reasonable. The wake evolves in both space and time, and one can only substitute one for the other provided the intervals are short compared with spatial or temporal evolution time-scales. This is often known as the 'frozen-flow' hypothesis: would the wake really be frozen in place as it convects through the measurement volume? The streamwise extent of the reconstructed wake, $X_w = UT_w$, where T_w is the wingbeat period, and here $X_w/c = 7.2$ for *G. s.* and 8.3 for *L. c.*

A comparison of near and far wakes in *G. s.* at $x = 3.2c$ and $19c$ (Johansson et al. 2008) shows that the qualitative and quantitative wake properties vary rather little with x and so the frozen flow assumption is tenable.

4.4 Drag, thrust and power

The power required to move at steady speed U is just DU, where D is the total drag that must be overcome to move through the surrounding fluid. In steady, unaccelerated flight, the total drag is balanced by the total thrust and the net horizontal momentum flux in the wake is zero. Although the wake is often touted as the footprint of the flying animal, which must contain a record of all the forces experienced by the wings and body, the causes and traces of drag and thrust are not necessarily separable. There are two major contributors to drag in a three-dimensional lifting system—the induced drag due to the downwash induced by the trailing vortices, and the viscous drag due to friction and pressure drag on all exposed surfaces. The induced drag is an inviscid component, and will be non-zero on all parts of the flyer that generate lift (and hence shed trailing vortices). The largest part of that, by far, can be expected to be from the wings, but especially in light of the complex root vortex shedding, it will be interesting to see how and when body lift makes a contribution to the induced drag.

The viscous drag is not predicted by any tractable theory, so it is always estimated from empirical performance curves, usually from polar plots of lift coefficient versus drag coefficient. There is a very significant uncertainty in its estimation, especially for complex systems like flapping bat wings. Given this practical problem, it is tempting to look to the wake structure for alternative measures of drag. Thus far, animal wake analyses have assumed that the total drag of the flying animal is balanced by a thrust that can be calculated from the geometry of the vortex wake (e.g. Spedding et al. 2003b; Hedenström et al. 2006; Henningsson et al. 2008). Thus the wake geometry, which is essentially an inviscid construct of line vortices in a potential flow, can be estimated to give a certain net forward impulse. This is then assumed to balance a viscous drag over one wingbeat, whose signature has not been explicitly measured, but which is assumed to trail behind the wings and body without disrupting the primary trailing vortex system.

It may be reasonable to further localize these forces. The wake directly downstream of the body presumably contains the drag signature of the body, and the measurement of a three-dimensional, mean streamwise velocity defect could be used to estimate the body drag. It is tempting therefore to look to data such as Fig. 6, which contains the velocity defect map for one wingbeat, for a complete solution to the

drag estimation problem. Indeed, blue and red blobs of momentum excess or deficit seem to be located in separate regions, and so while their sum must be zero, the different parts might be countable. It seems plausible that most thrust comes from the outer part of the wing, and that most drag comes from the body, as deduced from Fig. 6. However, it is far from clear that the pressure fluctuations can be ignored at $x = 3$–$5c$ in this highly unsteady wake, and it is also not clear whether appropriate far-field boundary conditions can be assumed. Furthermore, there is a uniqueness problem when the propulsor is a source of both thrust and drag, because there are an infinite number of combinations of negative and positive momentum flux that could have given rise to any given positive or negative net result. Teasing out these force components will be a significant challenge, but at least the data that one requires (such as Figs. 4, 6) are now becoming available.

4.5 Unsteady aerodynamics

Based on values of the Strouhal number alone ($St \approx 0.4$–0.5), we expect that unsteady aerodynamic forces are likely to be non-negligible. Wake measurements here show that $\Gamma/Uc \approx 1$ for both bat species and if this is interpreted as one half of a local lift coefficient (Rosén et al. 2007), then the wings apparently have time-averaged $C_L \approx 2$. A local wing section sees the vector sum of U and its local flapping speed, and not just U, and if the tip speed and mean speed have the same magnitude, then the corrected speed will be $\sqrt{2}U$ and the implied average C_L becomes 1.4. This is close to the upper limit that could be expected from moderate aspect ratio wings at this Re (Laitone 1997; Lyon et al. 1997; Spedding et al. 2008). *G. s.* has been shown to develop a significant fraction of its lift in near hovering flight from an unsteady leading-edge vortex (LEV) that appears and is stable due to wing accelerations (Muijres et al. 2008). It is possible that some form of LEV persists into higher speed conditions for *G. s.*, and since it appears to be flying in a very similar regime, the same extrapolation is as likely to hold for *L. c.* also.

5 Conclusion

The higher temporal resolution and availability of the third velocity component allows wake reconstructions for flying animals of greater detail and reliability than before. Nevertheless, it is notable how the new wake data are very consistent with previous reconstructions based on the painstaking assembly of multiple, separately-acquired data planes. We look forward to make new flight models based on these more comprehensive data, and to explore the challenges in estimating force coefficients from the 3D, unsteady wake.

Acknowledgments The manuscript benefited from the comments by two anonymous referees. The 3D high-speed PIV system was acquired through a generous grant from the Knut and Alice Wallenberg foundation. The research was funded by the Swedish Research Council to A.H.

References

Aldridge HDJN (1986) Kinematics and aerodynamics of the greater horseshoe bat, *Rhinolophus ferrumequinum*, in horizontal flight at various flight speeds. J Exp Biol 126:479–497

Brown RHJ (1948) The flight of birds. The flapping cycle of the pigeon. J Exp Biol 25:322–333

Ellington CP (1984) The aerodynamics of hovering insect flight. III. Kinematics. Phil Trans R Soc B 305:41–78

Hedenström A (2002) Aerodynamics, evolution and ecology of bird flight. Trends. Ecol Evol 17:415–422

Hedenström A, Spedding GR (2008) Beyond robins: aerodynamic analyses of animal flight. J R Soc Interface 5:595–601

Hedenström A, Rosén M, Spedding GR (2006) Vortex wakes generated by robins *Erithacus rubecula* during free flight in a wind tunnel. J R Soc Interface 3:263–276

Hedenström A, Johansson LC, Wolf M, von Busse R, Winter Y, Spedding GR (2007) Bat flight generates complex aerodynamic tracks. Science 316:894–897

Henningsson P, Spedding GR, Hedenström A (2008) Vortex wake and flight kinematics of a swift in cruising flight in a wind tunnel. J Exp Biol 211:717–730

Johansson LC, Wolf M, von Busse R, Winter Y, Spedding GR, Hedenström A (2008) The near and far wake of Pallas' long tongued bat (*Glossophaga soricina*). J Exp Biol 211:2909–2918

Laitone EV (1997) Wind tunnel tests of wings at Reynolds numbers below 70 000. Exp Fluids 23:405–409

Lindhe Norberg UM, Winter Y (2006) Wing beat kinematics of a nectar-feeding bat, *Glossophaga soricina*, flying at different flight speeds and Strouhal numbers. J Exp Biol 209:3887–3897

Lyon CA, Broeren AP, Giguere P, Gopalarathnam A, Selig MS (1997) Summary of low-speed airfoil data, vol 3. Soartech, Virginia Beach

Muijres FT, Johansson LC, Barfield R, Wolf M, Spedding GR, Hedenström A (2008) Leading-edge vortex improves lift in slow-flying bats. Science 319:1250–1253

Norberg UM (1976) Aerodynamics, kinematics, and energetics of horizontal flapping flight in the long-eared bat *Plecotus auritus*. J Exp Biol 65:179–212

Norberg UM (1990) Vertebrate flight. Springer, Berlin

Pennycuick CJ (1968) Power requirements for horizontal flight in the pigeon *Columba livia*. J Exp Biol 49:527–555

Pennycuick CJ (1975) Mechanics of flight. In: Farner DS, King JR, Parkes KC (eds) Avian Biology, vol 5. Academic Press, New York, pp 1–75

Pennycuick CJ (1989) Bird flight performance: a practical calculation manual. Oxford University Press, Oxford

Pennycuick CJ, Alerstam T, Hedenström A (1997) A new low-turbulence wind tunnel for bird flight experiments at Lund University, Sweden. J Exp Biol 200:1441–1449

Rayner JMV (1979a) A vortex theory of animal flight. Part 2. The forward flight of birds. J Fluid Mech 91:731–763

Rayner JMV (1979b) A new approach to animal flight mechanics. J Exp Biol 80:17–54

Rosén M, Spedding GR, Hedenström A (2007) Wake structure and wingbeat kinematics of a house-martin *Delichon urbica*. J R Soc Interface 4:659–668

Spedding GR (1987a) The wake of a kestrel (*Falco tinnunculus*) in gliding flight. J Exp Biol 127:45–57

Spedding GR (1987b) The wake of a kestrel (*Falco tinnunculus*) in flapping flight. J Exp Biol 127:59–78

Spedding GR, Hedenström A (2009) PIV-based investigations of animal flight. Exp Fluids. doi:10.1007/s00348-008-0597-y

Spedding GR, Rayner JMV, Pennycuick CJ (1984) Momentum and energy in the wake of the a pigeon (*Columba livia*) in slow flight. J Exp Biol 111:81–102

Spedding GR, Hedenström A, Rosén M (2003a) Quantitative studies of the wakes of freely flying birds in a low turbulence wind tunnel. Exp Fluids 34:291–303

Spedding GR, Rosén M, Hedenström A (2003b) A family of vortex wakes generated by a thrush nightingale in free flight in a wind tunnel over its entire natural range of flight speeds. J Exp Biol 206:2313–2344

Spedding GR, Hedenström A, McArthur J, Rosén M (2008) The implications of low-speed fixed-wing aerofoil measurements on the analysis and performance of flapping bird wings. J Exp Biol 211:215–223

Spedding GR, Hedenström A, Johansson C (2009) A note on wind-tunnel turbulence measurements with DPIV. Exp Fluids 46:527–537. doi:10.1007/s00348-008-0578-1

Warrick DR, Tobalske BW, Powers DP (2005) Aerodynamics of the hovering hummingbird. Nature 435:1094–1097